Journal of Power Sources 647 (2025) 237345

Contents lists available at ScienceDirect

Journal of Power Sources

journal homepage: www.elsevier.com/locate/jpowsour

Structure & composition of carbon fibers for electrochemical applications

Monja Schilling [a], Marc P. Vocht [b], Rafaela Debastiani [c,d], Simon Scherer [a,e], Frank Hermanutz [b], Roswitha Zeis [a,e,f,*]

[a] Karlsruhe Institute of Technology, Helmholtz Institute Ulm, Helmholtzstraße 11, D-89081, Ulm, Germany
[b] German Institutes of Textile and Fiber Research Denkendorf, Körschtalstraße 26, D-73770, Denkendorf, Germany
[c] Karlsruhe Institute of Technology, Institute of Nanotechnology, Kaiserstraße 12, D-76131, Karlsruhe, Germany
[d] Karlsruhe Institute of Technology, Karlsruhe Nano Micro Facility (KNMFi), Hermann-von-Helmholtz-Platz 1, D-76344, Eggenstein-Leopoldshafen, Germany
[e] Friedrich-Alexander-Universität Erlangen-Nürnberg (FAU), Faculty of Engineering, Department of Electrical Engineering, Cauerstraße 9, D-91058, Erlangen, Germany
[f] Department of Mechanical & Industrial Engineering, Faculty of Applied Science & Engineering, University of Toronto, 5 King's College Road, Toronto, Ontario, M5S 3G8, Canada

HIGHLIGHTS

- Nano-CT is visualizing the structural interior of the fiber.
- The fibers' structural integrity impacts the electrochemical cell stability.
- Probing structural properties of carbon fibers using WAXS.
- Different precursors influence the sizes of the graphite-type crystallites.

GRAPHICAL ABSTRACT

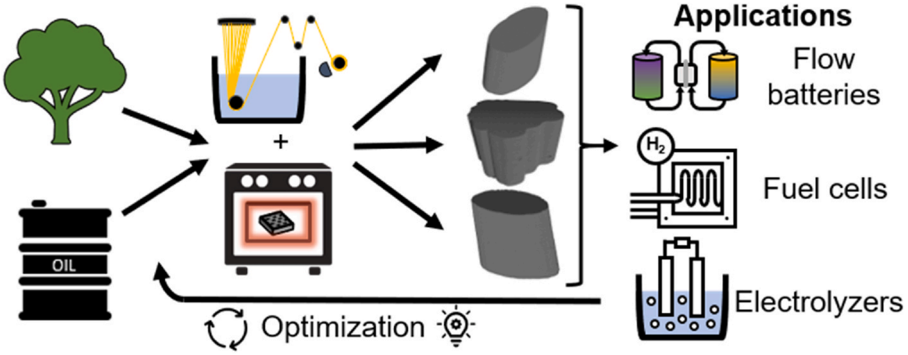

ARTICLE INFO

Keywords:
Vanadium redox flow battery
Manufacturing of carbon fibers
Thermal activation
Carbon-based electrode material
X-ray nano-computed tomography

ABSTRACT

Carbon-based electrode materials are used in a broad range of energy storage systems and influence their performance significantly. Electrode materials must be investigated to optimize the technologies' efficiency. This study examines lab-fabricated and commercial electrode materials for vanadium redox flow batteries (VRFBs), and the influence of thermal treatment on these materials. Scanning electron microscopy images and X-ray nano-computed tomography revealed significant differences between the 3D shapes of the carbon fibers, which are influenced by the choice of precursor material and manufacturing process. Both have a crucial influence on the inner structure of the fibers, such as holes, which lower the mechanical stability. Furthermore, the composition of the fibers was assessed using wide-angle X-ray scattering and X-ray photoelectron spectroscopy highlighting especially differences in the fibers' oxygen- and carbon content. The applied thermal treatment increased the O-content and thus enhanced the material's wettability, which was investigated with dynamic vapor sorption. No structural changes in the fiber shape were monitored after thermal treatment. The materials' electrochemical performance was studied for VRFBs. The study of different electrode materials here shows the importance of

---

* Corresponding author. Friedrich-Alexander-University Erlangen-Nürnberg (FAU), Faculty of Engineering, Department of Electrical Engineering, Cauerstraße 9, 91058, Erlangen, Germany.
E-mail address: roswitha.zeis@fau.de (R. Zeis).

https://doi.org/10.1016/j.jpowsour.2025.237345
Received 14 October 2024; Received in revised form 18 March 2025; Accepted 9 May 2025

choosing a suitable precursor and manufacturing process and the need for a multimodal characterization of materials to identify potential candidates.

1. Introduction

To tackle climate change, the emissions of greenhouse gases must be decreased as fast as possible. Renewable energy sources such as wind or solar offer an excellent solution to generate electricity without emitting undesired greenhouse gases. However, large-scale energy storage devices such as batteries, fuel cells, or electrolyzers are required to balance the fluctuations in the generation and use. The vanadium redox flow battery (VRFB) is a commercially available technology that allows the storage of energy on a large scale. The advantages of this technology are its long lifetime, high efficiency, low environmental impact, and fast response time [1,2]. A key part of any VRFB is the electrode due to its strong influence on the efficiency and its potential for degradation and aging [3–5]. Therefore, the electrodes need to be studied and improved. Typically, carbon fiber-based electrodes such as carbon felts, carbon papers, or carbon cloths, which have porosity and thus, a high surface area, are used [2,3,6]. The carbon materials are produced from various precursors, including natural resources such as cellulose [7–9] and petroleum-based sources resulting in e. g. polyacrylonitrile-based (PAN) carbon fibers [10,11]. The thickness and shape of the resulting fibers are influenced by the choice of precursor and the manufacturing process. Different techniques such as wet spinning or dry spinning give different results and can be used to optimize the fiber's shape [12–14].

The pristine carbon materials are often relatively hydrophobic and have a low catalytic activity towards the desired vanadium redox reactions [10,15–19]. Thus, pretreatment or modification of the materials is very common to improve wettability and electrochemical performance. A wide variety of methods have been proposed in the literature [20–24]; however, the standard procedure is based on a thermal treatment of the electrodes, which improves the wettability and catalytic activity by introducing functional groups, modifying the graphitic structure [10,15,16,18,22].

Carbon materials for VRFBs are often investigated using a variety of characterization techniques, as they must meet three crucial requirements for excellent performance: the electrode must have high catalytic activity to achieve a good electrochemical performance, a good wettability to effectively utilize the entire electrode area, and finally, a suitable structure to enable unimpeded flow of the electrolyte through the electrode. The electrochemical performance of electrode materials is often investigated using cyclic voltammetry (CV) and electrochemical impedance spectroscopy (EIS) to determine if the material is promising [4,15,17,25–27]. This is followed by full-cell testing to confirm the behavior and to study the material in a more application-oriented setup [28,29]. For pristine and thermally activated carbon fibers, the electrochemical performance is well-understood [15,17,18].

The structure of the electrode is often assessed using visualization techniques such as scanning electron microscopy (SEM) or atomic force microscopy (AFM), which provide 2D images of the sample [4,15,17,30,31]. However, the 3D structure of the electrode and its fibers is also crucial as the electrolyte must be pumped through the porous structure. Therefore, electrode materials are studied using X-ray μ-computed tomography (μ-CT) or X-ray nano-computed tomography (nano-CT) to examine the 3D structure at different resolutions. In these methods, X-rays are transmitted through the sample and acquired as projections, which allows for the reconstruction of the sample and its 3D visualization. μ-CT is used to resolve the structure of a larger section of the carbon material [32] which can be used, for example for pore network modeling [33]. In contrast, nano-CT is required to achieve higher resolutions. However, the published studies on carbon paper and electrospun fibers have not been able to resolve the detailed structure of the fibers such as kinks and edges on the fiber's surface or holes in the inner part of the fiber [34,35]. Additional information about the fiber can be obtained by X-ray crystallography [36,37] and wide-angle X-ray scattering (WAXS) [38], such as the graphitization degree, while elemental analysis [39,40] and Fourier transformation infrared spectroscopy [41,42] are used to study the composition of the fiber. In contrast, X-ray photoelectron spectroscopy (XPS) allows studying the elemental surface composition of the fiber [15,43]. For the last key property, the wettability of the carbon material, a laboratory-based approach can be chosen using dynamic vapor sorption (DVS) measurements, which investigate the hydrophilicity of the sample's surface. If more detailed information on the wettability of a large section is required and the flow through the porous structure needs to be studied, synchrotron X-ray imaging (radiography and tomography) experiments can be performed [4,16,44].

This study investigates different lab-fabricated and commercial electrode materials for use in electrochemical energy storage devices such as VRFBs and the influence of thermal treatment on the materials. The morphology of the fibers is studied with SEM and nano-CT highlighting the differences caused by the choice of precursor and manufacturing process. Additionally, WAXS and XPS are used to examine the composition of the fibers, and the wettability of the fibers is accessed using DVS, which shows significant differences in the wettability of the materials studied. Last, the electrochemical performance of the electrodes is investigated using CV and EIS combined with the distribution of relaxation times (DRT) analysis.

2. Experimental

2.1. Materials

For the lab-designed carbon fibers, air-gap spun cellulosic fibers (HighPerCell®) were used as carbon fiber precursors. They were synthesized using a solution of softwood pulp in the ionic liquid 1-ethyl-3-methylimidazolium octanoate ([C2C1im][Oc], IoLiTec, Germany) [8]. Additionally, ammonium tosylate (ATS) was synthesized by adding 1.5 equiv. of a 30 wt.-% aqueous solution of ammonia to an aqueous solution of p-toluene sulfonic acid, stirring for 2 h at room temperature, and then removing water in vacuo.

The air-dried pulp and [C_2C_1im][Oc] were mixed in a kneader for 30 min at room temperature. The obtained slurry was conveyed through a spiral pump at a rotational frequency of 100 Hz and degassed at 120 °C and 60 mbar in a thin-film evaporator (VTA GmbH & Co. KG, Aalen, Germany). The received solution was filled into a pressure filtration cauldron (Karl-Kurt Juchheim Laborgeräte GmbH, Bernkastel-Kues, Germany) using a heated gear pump (110 °C). The dopes contain 12 wt.-% of cellulose. Multifilaments were spun with a customized laboratory spinning device at 65 °C [8]. The spinning dope was passed through a filter with a mesh size of 0.043 mm. The solution was then extruded through a 250-hole spinneret with a capillary diameter of 150 μm. After passing an air gap of 10 mm, a water bath was used for coagulation. Filaments were washed with hot water (80 °C) by passing two baths and two washing godets. Before being wound onto a bobbin, fibers were dried with a heated godet (80 °C). Afterward, fabrics with a plain weaving design were prepared. A 0.35 M ATS solution was used for fabric finishing. The material was left within the solution for 2 h and afterward was left to air dry.

The ATS-finished fabric was carbonized under nitrogen atmosphere in a high-temperature batch type furnace (Gero HTK 8GR/22-1G) with a final carbonization temperature of 1300 °C applying a heating rate of 10 K/min. The obtained carbon cloth is called DITF_Pristine in the following.

The lab-designed carbon cloth will be compared in the following with the commercial carbon felts SIGRACELL® GFA 6.0 EA (in the following: GFA_Pristine) and GFD 4.6 EA (in the following: GFD_Pristine) from SGL Carbon (Meitingen, Germany). All three materials were thermally pretreated as proposed in the literature to enhance their wettability and electrochemical performance [15,19]. The carbon materials were placed in a covered glass Petri dish and heated to 400 °C for 25 h in a muffle furnace in an air atmosphere using a heating rate of 400 K/h.

2.2. Characterization

SEM: Scanning electron micrographs were recorded on a Zeiss Auriga field emission scanning electron microscope from Carl Zeiss (Oberkochen, Germany) using an acceleration voltage of 3.47 kV. All samples were sputter-coated with Pt/Pd before analysis.

Nano-CT: Carbon fibers were manually removed from the carbon electrode samples using tweezers and then affixed to a needle with UV-curing glue. The fibers were scanned using the lab-based nanoCT Xradia 810 Ultra, which employs a quasi-monochromatic X-ray beam from a Cr anode with an energy of 5.4 keV. This system operates with a sequence of optics to achieve a pixel size of 32.3 nm within a 16 μm field of view. The samples were scanned using the Zernike phase contrast mode over 180°, acquiring 901 projections with an acquisition time of 120 s per projection. The 3D data reconstruction was carried out using Zeiss' proprietary software, 'Scout and Scan Reconstructor', which is based on the filtered back projection algorithm.

For the 2D and 3D visualizations, a schematic workflow is displayed in Fig. 1 using the software Dragonfly [45]. After adjusting the greyscale, the slices were divided into areas with similar values on the greyscale using the 'Smart Grid Tool'. Next, the areas belonging to the fiber were marked (pink part in image) and used for the reconstruction resulting in a 3D display of the carbon fiber.

WAXS: WAXS measurements were performed on a D/Max Rapid II from Rigaku (Tokyo, Japan) operated at 30 mA and 40 kV using Cu $K\alpha$ radiation ($\lambda = 0.154059$ nm). A shine monochromator and an image plate detector were used. The scanning rate was 0.2°/min and the scanning step was 0.1°. All fibers were aligned in a fiber sample holder. The degree of crystallinity (X_c) was calculated according to the peak deconvolution method using Pearson-VII curves (Equation (1)).

$$X_c = \frac{\sum I_c}{\sum (I_c + I_a)} \tag{1}$$

I_c and I_a are the integrated intensities of the crystalline and the amorphous reflections, respectively. The crystallite size (t) was calculated according to Scherrer's equation [46].

$$t = \frac{K\lambda}{B \cdot \cos\theta_b} \tag{2}$$

B is the width at half-height of the reflection, K is the Scherrer factor, which depends on the crystallite shape, and θ_b is the Bragg angle.

XPS: XPS measurements were carried out with a Specs XPS system using monochromatized Al Kα radiation (300 W, 15 kV) and pass energies of 90 eV and 30 eV for survey and detail measurements, respectively. The software CasaXPS was employed for the peak fit of the XPS results. A Shirley-type background was used in all cases. While an asymmetric line shape was inserted for the sp^2-carbon peak in the C1s detail spectra, a (symmetric) Gaussian-Lorentzian peak shape was used for all other peaks. Survey spectra and exemplary fits are displayed in the supporting information.

DVS: DVS measurements were performed with a Q5000 Sorption Analyzer (TA Instruments) to study the wettability of the carbon materials. The sample is heated up to 60 °C for 90 min at the beginning and for 300 min at the end of the measurement to remove water residues. The measurement itself was conducted at 25 °C. After an initial step at 0 % relative humidity (RH) for 300 min, the RH was increased to 30 % for 1200 min. Afterward, 0 % RH was kept for 300 min before heating the sample.

iGC: The inverse gas chromatography (iGC) measurements to determine the surface area were performed with a IGC Surface Energy Analyzer (SMS, Surface Measurement Systems Ltd.) equipped with a flame-ionization detector. The sample was packed in silanized glass chromatographic column (SMS Ltd.) with an inner diameter of 4.0 mm. Plugs of silanized glass wool (Superlco®, Sigma-Aldrich) were used to fixate the sample in the column. For all measurements, N_2 (99.999 %, Westfalen AG) was used as carrier gas at a flow rate of 10 mL min^{-1}, and methane (99.95 %, Air Liquide) as reference. All alkanes (n-heptane, n-octane) used were HPLC grade and purchased from Thermo Fisher Scientific. The DITF_Pristine and GFD_ThermAct were preconditioned in the column at 110 °C under nitrogen flow for 1 h to remove residual water. The measurements were carried out at sample-dependent temperatures to obtain accurate results: DITF samples at 20 °C, GFA pristine at 30 °C, and activated at 60 °C. Before applying the BET method, its applicability was checked via the type of adsorption isotherm.

CV: CV measurements were performed to investigate the electrochemical performance of the electrode materials using a three-electrode setup with an in-house developed flow cell [26] and an SP-300 potentiostat (BioLogic Science Instruments). The electrodes were cut into rectangular pieces (1.0 cm × 1.0 cm) and were placed in the working electrode (WE) of the flow cell's channel and contacted by a gold foil (0.25 mm, 99.9975+ %, Alfa Aesar) and a gold wire (Ø 0.5 mm, 99.9975+ %, Alfa Aesar). In all experiments, an in-house developed hydrogen reference electrode (RHE) was used as the reference electrode (RE), and a stack of three thermally activated carbon papers (2.5 cm × 2.5 cm) served as the counter electrode (CE). The carbon paper stack was contacted with a titanium foil (1.0 mm, 99.2 %, Alfa Aesar) and a gold wire. The CVs were conducted at room temperature with a scan rate of 2 mV s^{-1} while no flow was applied. Potential limits were chosen so the peaks were evident during the anodic and cathodic scans.

EIS: EIS characterized the wettability and processes in the positive half-cell using the same setup as for the CV measurements [26]. The EIS

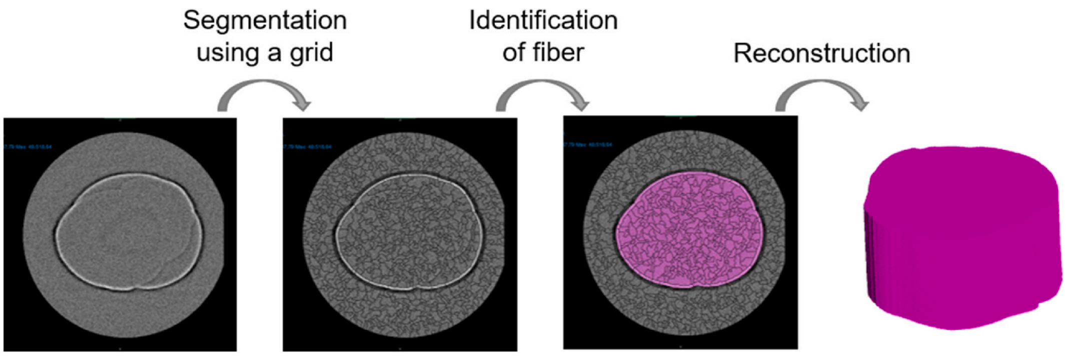

Fig. 1. Schematic display of the segmentation process for analyzing nano-CT data.

measurements were performed at room temperature at a flow rate of 15 mL min^{-1} in a frequency range from 100 kHz to 3.5 mHz. The potentiostatic mode was used with a single sinusoidal excitation of 5 mV as the perturbation and an applied potential of 1.05 V vs. RHE. During the measurement, the electrolyte was pumped from the electrolyte reservoir through the flow cell and back to the reservoir by a peristaltic pump (Masterflex L/S®, Cole-Parmer). Since the conditions at the electrodes should remain constant to gain meaningful impedance data, the electrolyte was continuously pumped to ensure a steady state [25,26].

The data were further analyzed using a MATLAB-based tool called 'DRTtools' [47] based on the Tikhonov regularization. The spectra fitting is based on a Gaussian function for the discretization and includes the inductive data. A regularization parameter of E−9 was used.

3. Results and discussion

Three different carbon-based electrode materials are studied before and after thermal activation and the results are presented in three sections. The first section discusses the fiber shapes and morphology, the second one the fiber composition, followed by a discussion of the fiber wettability and electrochemical performance of the electrode material.

3.1. Fiber shapes

The structure and morphology of the electrode material influence the overall performance of electrochemical devices significantly since the electrode material serves as catalyst (e.g. VRFBs) or as support material for the catalyst (e.g. fuel cells) and as the current collector, and distributes the electrolyte or reaction gases within the electrode. Thus, the materials and their carbon fibers need to be studied in detail to be optimized for the respective application. Here, the carbon fibers of commercially available and lab-fabricated carbon-based electrode materials for VRFBs are studied using SEM and nano-CT allowing us to investigate the surface of the fibers and their internal structure. Besides, the knowledge about the fibers and the resulting electrode material for VRFBs can be transferred and used to optimize other electrochemical applications such as fuel cells or electrolyzers since the precursors and resulting fibers are often similar.

Fig. 2 shows representative images of the studied electrode materials. In each image, several carbon fibers and their surface structure are visible in SEM images. The fibers DITF_Pristine and DITF_ThermAct (Fig. 2a and b) have both smooth surfaces with some inhomogeneities, which could be caused by impurities. After the thermal activation, the number of inhomogeneities is lower. The diameter of roughly 10 μm and the roundish shape of the fibers does not change during activation. Further insights into the 3D shape of the fiber will be presented later (Fig. 3).

In contrast, the fibers of the commercial material GFA have a different structure. The fibers themselves consist of an inhomogeneous bundled rod structure for both, pristine and thermally activated fibers (Fig. 2c and d). Thus, the fiber has a high number of kinks and edges, which are considered defect sites since they foster undesired side reactions such as hydrogen evolution or carbon corrosion in VRFBs as recent studies demonstrated [5,48]. During the thermal activation, the shape and surface of the fibers does not change. The DITF- and GFA-fibers are both based on a cellulose precursor, but their fabrication process differs. The fibers are obtained by using a cellulose-containing solution, which is spun into another solution, the so-called coagulation bath. In the case of the GFA fibers, the chemically modified cellulose in a basic solution is spun directly into an acidic solution, which creates a structure like bundled rods [49]. In contrast, the roundish fibers can be achieved by choosing a cellulose solution based on ionic liquids, which is spun via an air-gap into water [8]. The spinning process with an air-gap always leads to roundish fibers since the structure with the smallest surface is favored. Furthermore, the ionic liquid used in the precursor solution has a larger solubility for cellulose and thus, higher concentrations can be reached, which are favored. Additionally, the used ionic liquid is non-toxic, available on an industrial scale, and can be reused in the manufacturing process, which lower the production costs. In general, this indicates that the manufacturing process and conditions need to be chosen carefully.

The third material, the GFD-fibers, is based on PAN, derived from

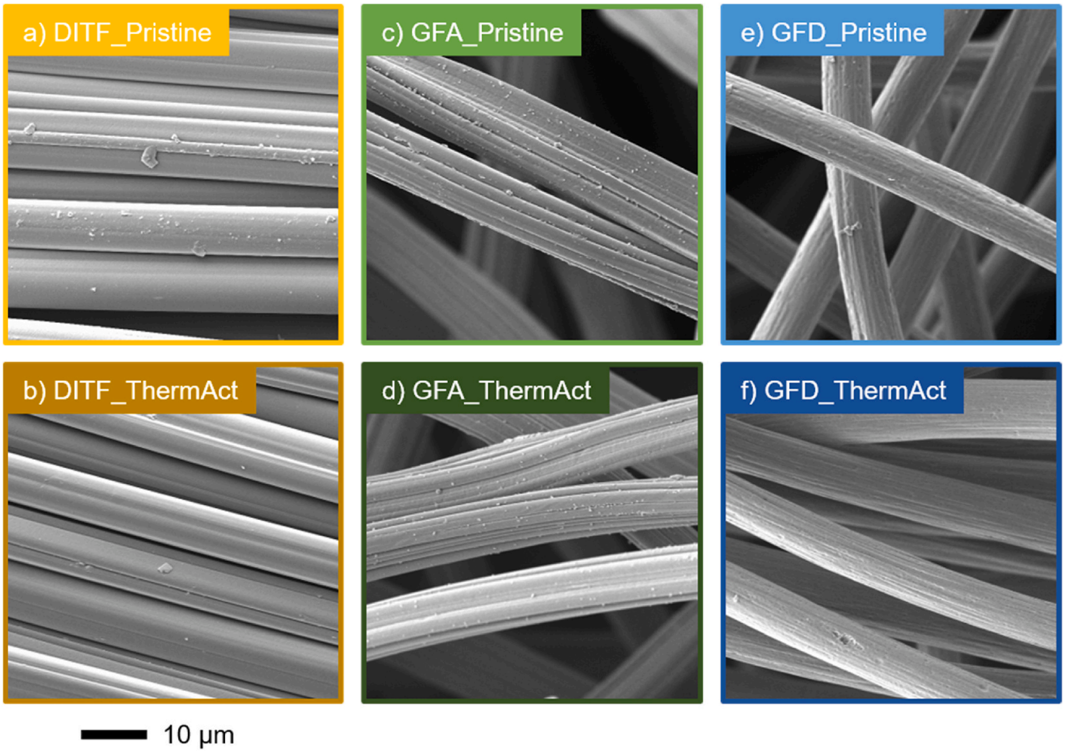

Fig. 2. SEM images of different electrode materials before and after thermal activation.

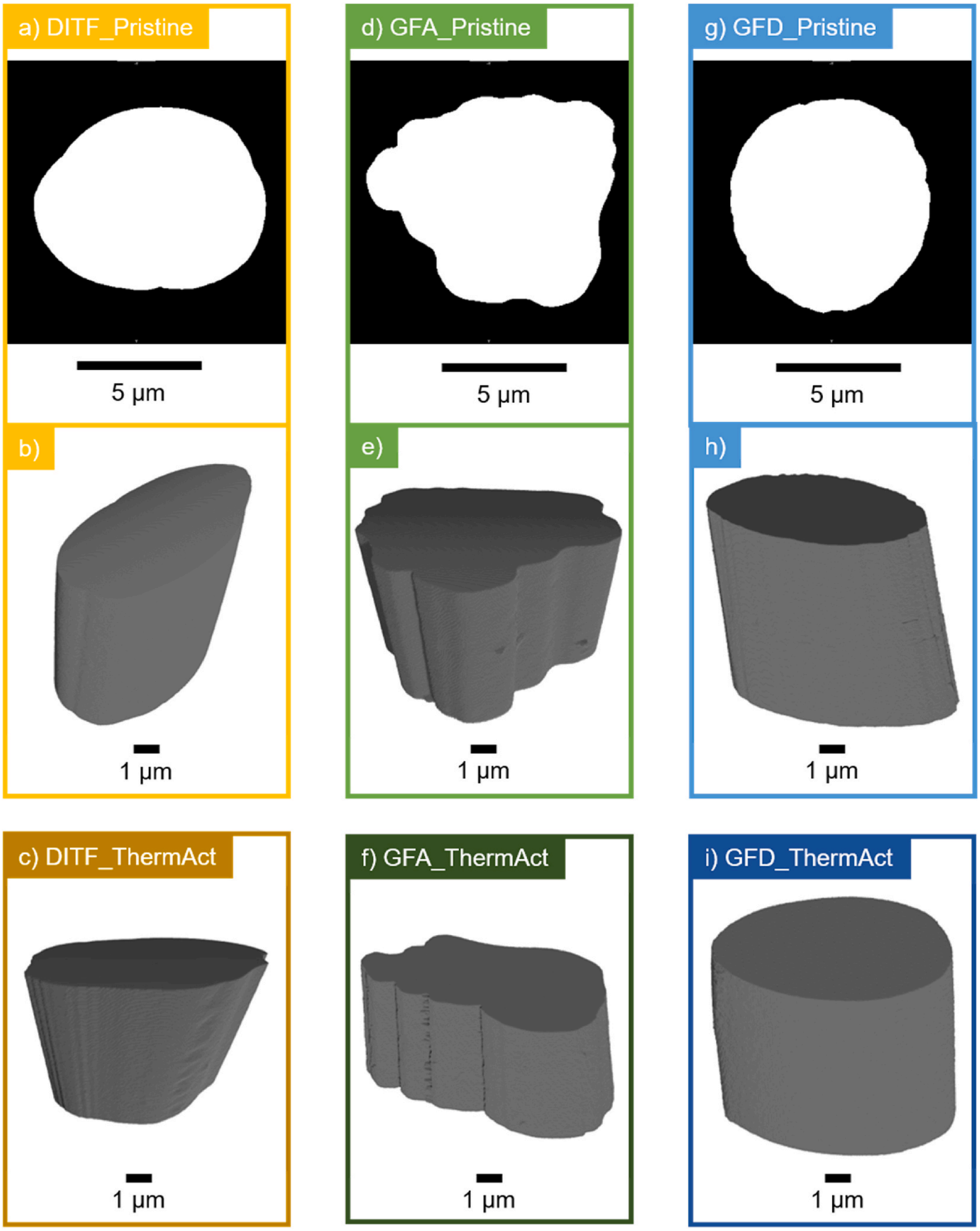

Fig. 3. Nano-CT images of different electrode materials prior to and after thermal activation: a), d), and g) slices through fiber cross-section, and b), c) e), f), h), and i) 3D images of fibers.

petroleum. These fibers are fabricated using a PAN-containing organic solution and are directly spun into the coagulation bath [13]. SEM images of GFD_Pristine and GFD_ThermAct displayed in Fig. 2e and f shows these fibers have a roundish shape and some macroscopic pores at the surface, in contrast with the roundish DITF-fibers that have a smooth surface and are free from macroscopic pores. Again, the morphology of the fiber is unchanged after thermal activation.

The strong influence of the different precursors and manufacturing routes is even better visible in the obtained 3D displays of the fibers using nano-CT. To the best of our knowledge, this is the first time individual fibers including their inner structure for electrochemical applications are studied using nano-CT with a high resolution. For the measurements, an individual fiber is extracted from the electrode material. The obtained cross-section slices are segmented to distinguish between the fiber and the surroundings (Fig. 3a–d, and g). Similar slices are obtained for each material before and after thermal activation. Therefore, the cross-section slices are only shown for the pristine materials. Additionally, 3D representations are reconstructed based on the segmentation, which highlights the 3D shape and morphology of the fiber (Fig. 3b, c, e, f, h, and i).

The cross-section slice of DITF_Pristine (Fig. 3a) shows a roundish fiber with a diameter of 8 µm–10 µm. The SEM images revealed a smooth surface and here, the cross-section slice has only minor kinks, e. g. at the bottom part of the fiber. The 3D representations of the DITF_Pristine (Fig. 3b) and DITF_ThermAct (Fig. 3c) highlight the smooth morphology and roundish shape of the fibers, with no significant differences observed between the pristine and activated fibers. Thus, the fiber is not destroyed during the activation step by oxidation of the carbon material in air under the applied conditions. The inner part of the DITF fibers is dense and does not consist of any inhomogeneities or holes. Thus, this material is very suitable for use in electrochemical devices such as VRFBs, since the fiber has a smooth surface with very few kinks or edges, which helps to suppress the HER [48], and promises high mechanical stability at the same time. To achieve this, the DITF-fibers were carbonized using ATS to increase the carbon yield and minimize the defects of the carbon fiber material [50].

Despite the fiber being based on the same precursor, cellulose, the shape of the GFA-fiber differs significantly from the DITF-fiber, which is caused by the choice of manufacturing process [8,9,49–51]. The cross-section slice in Fig. 3d displays the bundled rod structure in more detail. The slice shows the uneven shape of the surface, which consists of many kinks and edges. The defect-rich surface leads to more side reactions since potential spikes occur at the defects. Additionally, the roughly 10 μm thick fiber has a high number of small holes in its inner part. The holes are not depicted in Fig. 3 since they are discussed in more detail later in Fig. 4. The presence of holes in the fiber leads to significant mechanical stability issues since the carbon fiber will always break at its weakest point such as a hole or kink [52,53]. Besides the spinning process used for precursor manufacturing, the carbonization conditions have a significant influence on the carbon fiber properties, both mechanical and structural.

Although the GFA_Pristine and GFA_ThermAct have both the above-mentioned bundled rod structure, the shape of the fibers is not identical. The GFA_ThermAct has an oval shape compared to the more roundish GFA_Pristine. However, the variations are caused by the manufacturing process and not by the thermal activation. In the SEM images (Fig. 2c and d), variations in shape are also visible. This fiber exhibits several of the disadvantages above-mentioned for use in electrochemical applications, such as an inhomogeneous morphology including kinks and edges [5,48], and a lower mechanical stability caused by the holes inside the fiber [50].

The third investigated material, GFD, is a commercial carbon felt for VRFB electrodes. As already visible in the SEM images (Fig. 2e and f), the surface of GFD has some macroscopic defects – dents – at its surface in the range of <1 μm. The fiber itself has a diameter of roughly 8.5 μm and a round cylindrical shape. The same observation as for the other materials was made here, the 3D structure is not influenced by the thermal activation under the selected conditions. The GFD-fibers have a dense inner part and no holes, which is beneficial for mechanical stability.

In conclusion, the shape of the fiber is significantly influenced by the choice of precursor and fabrication process. Even small changes can lead to differences in the morphology and structure of the fibers. For use in electrochemical devices, fibers with a smooth surface free of inhomogeneities and defects and a dense inner part are favorable.

The DITF- and GFD-fibers have a dense inner part and no holes, whereas the GFA fiber has a structure with cavities. The high-resolution

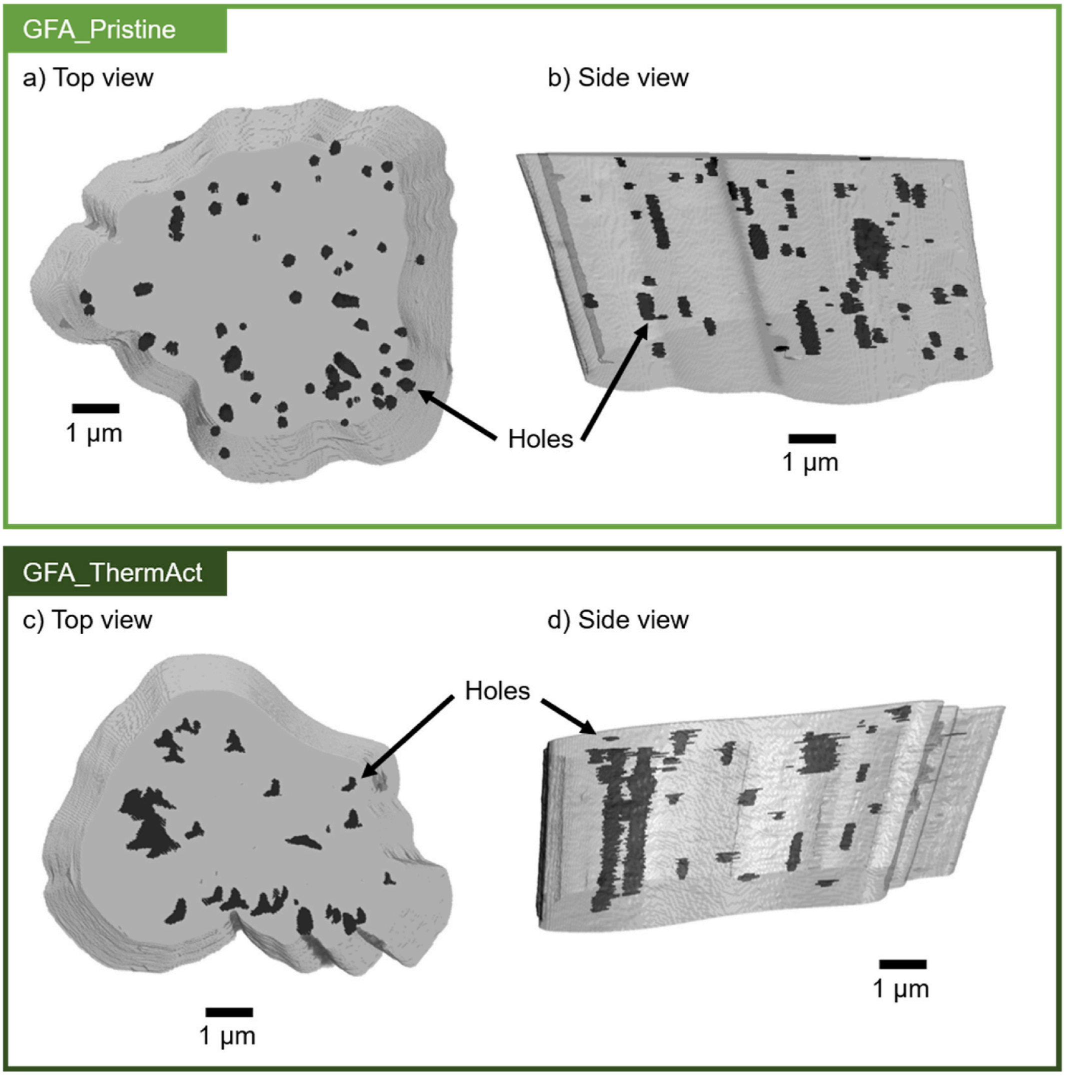

Fig. 4. 3D representations of a), b) GFA_Pristine and c), d) GFA_ThermAct displaying the holes in the inner part of the fibers in different views.

nano-CT measurements allow to resolve imperfections in the size below 1 μm in the inner part of the fiber. In Fig. 4, the holes inside GFA-Pristine and GFA_ThermAct are shown. The fibers are each displayed in the top view and the side view to highlight the positions of the holes in the 3D structure of the fiber.

The GFA_Pristine fiber has a high number of small holes inside its structure. The top view (Fig. 4a) shows that the holes are present in the whole fiber cross-section, but more condensed in the bottom part of the image. Several of the holes are also close to the surface of the fiber, especially in the left part of the fiber. Most holes have a round shape and only a few have an oval or line-like shape. The side view (Fig. 4b) highlights this even more. In contrast, the GFA_ThermAct fiber consists of a lower number of cavities, which are often close to the surface of the fiber (especially at the bottom part in Fig. 4c) and have a triangular shape. The side view (Fig. 4d) reveals that the holes in the left part of this image (marked by the arrow) reach through the whole scanned region.

We believe that the strong differences in the shape, size, and number of holes are not caused by the thermal activation but by the manufacturing process, which leads to different fiber shapes and thus, also different hole patterns in the inner part of the fiber. Vocht et al. [50] studied cellulose-based carbon fibers, which are manufactured using different processes and processing conditions. They observed similar holes in cross-sectional SEM images and concluded that the manufacturing process and choice of precursor and conditions influence the inner and outer structure of the fiber significantly. Since the manufacturing process is complex and sensitive to changes (such as temperature during stabilization or carbonization), the conditions must be carefully controlled to guarantee a reliable product.

Nevertheless, holes in the fiber are undesirable since they lead to a lack of mechanical stability. The “weakest link theory” of Weibull predicts that a brittle material such as a carbon fiber will always break at its weakest point [52,53]. Defects such as holes, kinks, and edges act as macroscopic defect sites, whereas imperfections in the carbon structure act as microscopic defect sites. Both defect types result in a higher chance that the fiber will break during operation since carbon materials are usually compressed in the electrochemical cells to enhance the electrical contact. Furthermore, the imperfections can lead to cracks at the fiber’s surface and the electrolyte can wet the inner structure of the fiber. Since any imperfections in the structure such as kinks and edges lead to potential spikes, more undesired side reactions such as carbon corrosion or hydrogen evolution in VRFBs are fostered. Recently performed synchrotron X-ray imaging experiments highlight the influence of the materials and fiber shape on the hydrogen evolution reaction [48]. Less amount of hydrogen volume was formed using an electrode with smooth fiber surfaces compared to an irregular shaped one such as the GFA_fiber. Thus, imperfection-free carbon fibers are required to allow long-term operation of electrochemical devices such as VRFBs.

3.2. Fiber composition

The fiber composition is a key parameter that influences the performance of electrochemical devices as well as the shape of the carbon fiber. In this section, the structural composition will be investigated using WAXS, and the elemental composition using XPS.

WAXS measurements allow to characterize the graphite-type crystallites, every carbon fiber consists of, and to learn more about crystal dimensions. During the measurements, the scattered X-rays at a distance far from the primary beam are monitored. The obtained diffraction patterns and resulting diffractograms are shown in the supporting information (Fig. 9). Based on the fitting of the curves, crucial parameters are calculated, which characterize the structural composition of the material. For an easier understanding, the meaning of the parameter is explained using the scheme in Fig. 5. The size of the graphite-type crystallites is determined by L_a and L_c, which give the length and height of a crystallite in and across the fiber axis, respectively. Based on the interlayer distance $d_{(002)}$ and the number of layers N_c stacked in a graphite-like type, information about the electrical conductivity can be drawn. A high value for N_c and a value close to the value for the distance of the graphene layers in graphite ($d_{(002),\ graphite} = 0.355$ nm [54]) hints at good electrical conductivity of the individual fiber [55].

The calculated values for the above-mentioned parameter are summarized in Table 1 for all carbon materials before and after thermal activation. Only small deviations between the pristine fiber and thermally activated fiber of each material were observed. The calculated interlayer distances $d_{(002)}$ are in the typical range for carbon fibers of 0.34 nm–0.36 nm for all studied materials [56]. As mentioned above,

Table 1
Structural properties of carbon fibers using WAXS.

Sample	L_c/nm	L_a/nm	$d_{(002)}$/nm	N_c
DITF_Pristine	1.03	4.15	0.354	2.9
DITF_ThermAct	1.01	4.26	0.350	2.9
GFA_Pristine	1.19	5.21	0.354	3.4
GFA_ThermAct	1.27	5.10	0.356	3.6
GFD_Pristine	2.54	6.45	0.350	7.3
GFD_ThermAct	2.34	6.97	0.349	6.7

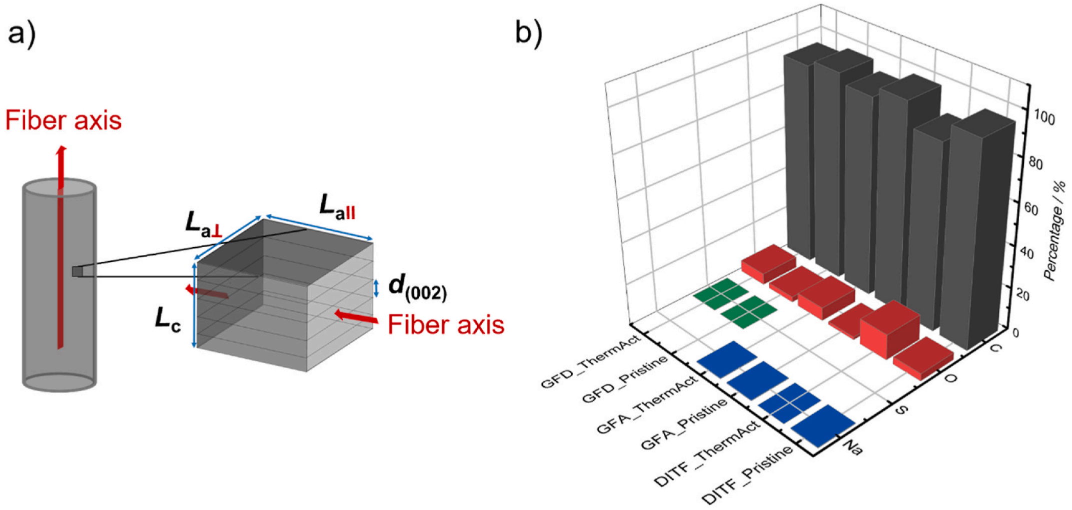

Fig. 5. a) Scheme highlighting the parameters obtained for WAXS measurements, and b) analysis of the XPS measurements: display of the elemental composition of different electrode materials prior and after thermal treatment.

this hints that the electrical conductivity of the carbon fibers is excellent. A significant difference between the materials fabricated from different precursors is found in the sizes of the graphite-type crystallites. The DITF-fibers and GFA-fibers are fabricated both from cellulose and have a significantly lower value for L_c compared to the fiber fabricated from PAN (GFD-fibers). The number of layers N_c is calculated based on this value. PAN fibers have roughly twice as many graphite-type stacked graphene layers in their crystallites as cellulose-based fibers. The mechanical stability of the fibers is influenced by the number of defects based on the "weakest link theory" [52,53] and imperfections such as borders between the individual crystallites act as microscopic defects. Thus, a high number of stacked layers is favorable.

WAXS allows to study the structural composition, whereas XPS measurements deliver more information about the elemental composition of the surface. The survey spectra and exemplary detail scans of DITF_Pristine including corresponding peak fits are shown in the supporting information (Fig. 10). Fig. 5 displays the calculated elemental compositions of the carbon materials. All fibers consist mainly of carbon, ranging from 87.7 % (DITF_ThermAct) to 98.4 % (GFA_Pristine), followed by the content of oxygen, which is relevant for the wettability of the material. Additionally, the cellulose-based carbon materials consist of sodium as an impurity (max. 0.4 %), which is introduced during the fabrication process. In contrast, the GFD-fiber is petroleum-based and has thus, sulfur impurities since the raw oil consists of it (max. 0.1 %).

Significant differences in their oxygen content between the samples were noticed. The GFA_Pristine has an O-content of 1.3 %, whereas the O-content for the thermally activated fiber is roughly 5 times larger (6.3 %). The DITF_Pristine fiber already has an O-content of 3.5 %, but the value only increases by a factor of 3.5 during the thermal activation (O-content of DITF_ThermAct: 12.3 %). In contrast, the O-content of GFD-fibers increased during the thermal activation only by a factor of two (O-content of 2.5 % for GFD_Pristine vs. 5.4 % for GFD_ThermAct).

3.3. Fiber wettability

Another crucial parameter influencing the performance of electrochemical devices is the wettability of the material. Depending on the choice of application, the wettability needs to be optimized to fit the needs. In the case of VRFBs, electrode materials, which can easily be wetted, are favorable since the carbon material acts as a catalyst for the electrochemical reaction and guides the electrolyte through the material [4,16,44,57]. If the material is hydrophobic, a large pressure drop is observed, which lowers the overall efficiency of the VRFB. Wettability can be investigated using two different methods. First, synchrotron X-ray imaging experiments are used to study the wettability and electrolyte distribution in the electrode [4,16,57,58]. However, synchrotron experiments are often complex to analyze, costly, and require extensive preparation time and work. Thus, another approach is needed for day-to-day experiments in the lab. DVS measurements provide exactly this and deliver information about the wettability of the material by measuring the weight change of a sample at different relative humidity. In the experiments conducted, the RH was increased from 0 % to 30 % and afterward decreased to 0 % again and significant differences between the materials studied were observed (Fig. 6).

DITF_Pristine shows a weight change of 2.5 % during the adsorption process and the equilibrium is reached slowly. During the desorption, the initial weight is reached slowly. In contrast, after thermal activation, the DITF_ThermAct has a weight change of 7.2 %. Both, during the desorption and adsorption, the equilibrium is reached quickly. XPS experiments revealed that the DITF_Pristine has a high amount of hydrophilic oxygen-containing functional groups, which is even increased after thermal activation.

The commercial materials, GFA and GFD, have a significantly lower wettability before and after thermal activation. For better visibility, a zoom-in on the respective data is presented in Fig. 6b. The pristine GFA and GFD do not adsorb any water at 30 % RH (weight change of 0.00 %). After the thermal activation, which introduces polar functional groups, the wettability is only slightly improved and leads to weight changes of 0.03 % and 0.01 % for GFA and GFD, respectively.

For VRFBs, good wettability is crucial to enhance the performance of this type of battery. Thus, the DITF-fibers are very promising. Furthermore, the DITF_Pristine is already very hydrophilic and could therefore be used in commercial VRFBs without an additional activation step. This saves time and costs in large-scale production.

3.4. Electrochemical performance

CV and EIS studies were performed to characterize the electrochemical performance of the electrode materials in the positive half-cell of a VRFB. Since the pristine commercial carbon felts (GFA_Pristine and GFD_Pristine) are reported to show a low catalytic activity towards the vanadium redox reaction [15,17,22] and a thermal activation step is a common procedure for carbon-based electrodes [17,18,59,60], only the CVs and EIS spectra of the thermally activated materials are included in

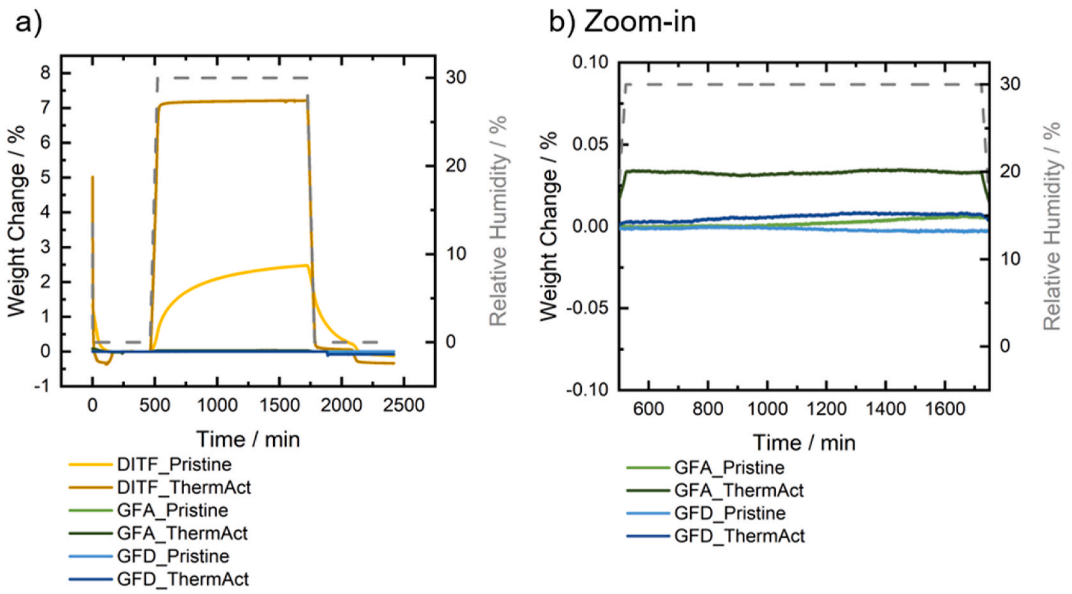

Fig. 6. Water vapor sorption and desorption experiments at 0 % RH and 30 % RH for a) all samples and b) zoom-in for selected samples.

this publication. The electrodes have different thicknesses and different area weights. Thus, the BET surface area of the materials was determined using iGC. The current values in the CVs are normalized by the BET surface area to allow better comparison and given in mA per $m^2\ g^{-1}$. GFA_ThermAct has a BET surface area of 3.10 $m^2\ g^{-1}$ and GFD_ThermAct of 0.91 $m^2\ g^{-1}$. The DITF_Pristine shows a significantly lower BET surface area of 0.35 $m^2\ g^{-1}$.

The resulting CVs are displayed in Fig. 7. All materials show the characteristic duck shape and symmetrical peaks during the anodic and cathodic scan. The charge ratio of the anodic and cathodic scan $C_{anodic}/C_{cathodic}$ is similarly high for all three materials with 96 % for DITF_Pristine and GFA_ThermAct, and 97 % for GFD_ThermAct. Thus, the vanadium redox reactions are reversible and the materials are suitable for VRFB electrodes. Furthermore, we analyzed the peak-to-peak separation ΔE. The DITF_Pristine has the smallest peak-to-peak separation with 169 mV, compared to 332 mV for GFA_ThermAct and 245 mV for GFD_ThermAct. Thus, the DITF_Pristine shows lower overpotentials, and charging and discharge during full-cell measurements would lead to better efficiencies. For commercial applications, the costs for electrodes need to be low. Fewer steps during production are favored. The DITF_Pristine shows a better performance regarding peak-to-peak separation and similar currents (normalized based BET area using iGC) compared to the thermally activated electrodes. Thus, the DITF materials are interesting for commercial application since costs are reduced if no thermal activation is required.

Furthermore, we characterized the electrochemical performance of the electrodes using EIS measurements combined with the DRT analysis (Fig. 8). DRT analysis is a well-suited tool to assign peaks in a DRT spectrum to physical processes and to study the effects of different conditions, 3D structures, or materials. Our group established this analysis tool for VRFB research, identifying processes in three different frequency ranges in various DRT spectra. The high-frequency (HF) range provides information about the electrochemical reaction, whereas the mid-frequency (MF) range helps to investigate the transport processes in the porous structure of the electrode. We can determine additional information about ion transport based on the impedance in the low-frequency (LF) range [26]. DRT analysis is also used to link the material's wettability to its surface morphology [4,17,61]. Again, we studied DITF_Pristine and the thermally activated materials GFA_ThermAct and GFD_ThermAct.

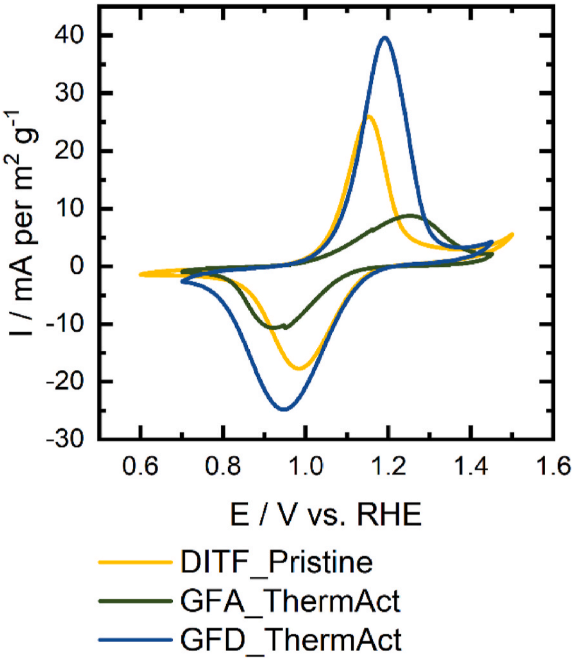

Fig. 7. CV measurements of electrode materials in a flow cell in 0.1 M V^{4+} in 2 M H_2SO_4 with 2 mV s^{-1}. The current was normalized using the BET surface area obtained by iGC for each material.

The GFD_ThermAct showed the lowest water uptake during the DVS measurements and the DRT analysis confirms the low wettability of the material. The material shows a very high impedance related to the MF range. Thus, the pumping through the material is hindered. Both commercial materials are fabricated using a needle-punch manufacturing technique. Since the GFA_ThermAct shows a significantly lower impedance in the MF range, the high impedance of GFD_ThermAct can be attributed to its poor wettability. The DITF_Pristine shows a general peak shift to lower frequencies and a slightly different distribution over the frequency range. This is caused by the different 3D structure of the electrode since the material is fabricated using weaving.

The EIS and DRT analysis demonstrate the strong influence of the electrode's 3D structure. For optimization studies, not only the catalytic activity but also the wettability and 3D structure need to be taken into consideration.

4. Conclusion

In this study, we characterized different lab-fabricated and commercial electrode materials for electrochemical applications such as VRFBs. Furthermore, a standard pretreatment in VRFB research, a thermal activation in air, was applied to the materials to increase their wettability, which led to no significant structural changes in the fiber shape but to a change in functional groups at the fiber surface.

Fibers based on a PAN-precursor have a round shape with macroscopic pores at the surface. The inner part of the fiber is dense without any holes, leading to higher mechanical stability. The WAXS measurements showed for GFD_Pristine and GFD_ThermAct that the materials are promising to have high electrical conductivity, which is desired. However, both materials have poor wettability – even after the thermal activation step.

The second commercially available fibers studied are fabricated from a cellulose-based precursor, which influences the fiber shape and surface significantly. In simulation work, it is often assumed that the fibers are perfect cylinders. However, the GFA-fibers have inhomogeneous surfaces with a bundled rod structure leading to many kinks and edges, which foster undesired side reactions and are far from the ideal cylinder. Additionally, the fibers have several holes in their inner structure, which lowers the mechanical stability. Again, the commercial material exhibits a low wettability, which decreases the efficiency of e.g. VRFBs due to a large pressure drop in the electrochemical cell.

Additionally, the lab-fabricated fiber DITF_Pristine, based on a cellulose precursor and fabricated via a different manufacturing process as the GFA-fiber, was studied. SEM and nano-CT revealed round, cylindrical fibers with a dense inner part. No holes in the fiber were found using nano-CT, proving the high mechanical stability of the carbon fibers. Additionally, the DITF_Pristine fiber has already excellent wettability. Thus, no additional thermal activation step or other pretreatment is required for the use as electrode material in VRFBs, which saves time and costs during the production process. Furthermore, the DITF_Pristine shows better catalytic activity than the thermally activated commercial material, proving its suitability for VRFBs.

The conducted study of different electrode materials shows the importance of the multimodal characterization of materials to identify potential candidates and optimize them for use in electrochemical devices to achieve high efficiencies.

CRediT authorship contribution statement

Monja Schilling: Writing – original draft, Visualization, Methodology, Investigation, Formal analysis, Data curation. **Marc P. Vocht:** Writing – review & editing, Visualization, Methodology, Investigation, Formal analysis, Data curation. **Rafaela Debastiani:** Writing – review &

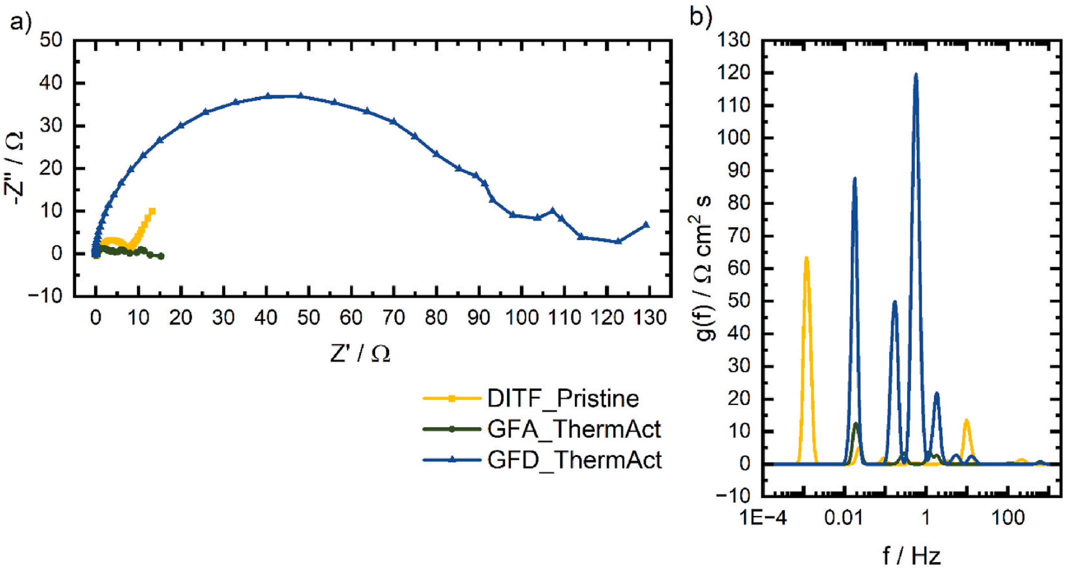

Fig. 8. a) Nyquist plots and b) DRT spectra of electrode materials in a flow cell under a constant flow of 15 mL min^{-1}. An electrolyte with 0.1 M V^{4+} in 2 M H_2SO_4 was used and a potential of 1.05 V vs. RHE was applied.

editing, Visualization, Investigation, Data curation. **Simon Scherer:** Writing – review & editing, Methodology, Investigation. **Frank Hermanutz:** Writing – review & editing, Supervision, Project administration, Funding acquisition **Roswitha Zeis:** Writing – review & editing, Supervision, Project administration, Funding acquisition, Conceptualization.

Declaration of competing interest

The authors declare that they have no known competing financial interests or personal relationships that could have appeared to influence the work reported in this paper.

Acknowledgments

We especially thank SGL Carbon for supplying the SIGRACELL® carbon felts, and Dr. Thomas Diemant for the XPS measurements. M.S. gratefully acknowledges financial support through a Kekulé Ph.D. fellowship by the Fonds der Chemischen Industrie (FCI) and from the support programs for female researchers by Ulm University. This work was partly carried out with the support of the Karlsruhe Nano Micro Facility (KNMF, www.knmf.kit.edu), a Helmholtz Research Infrastructure at Karlsruhe Institute of Technology. The Xradia 810 Ultra (nanoCT) core facility was supported (in part) by the 3DMM2O - Cluster of Excellence (EXC-2082/1390761711). R.D. acknowledges the support of the Cluster of Excellence 3DMM2O (EXC_2082/1–390761711) funded by the German Research Council (DFG). This work contributes to the research performed at CELEST (Center for Electrochemical Energy Storage Ulm-Karlsruhe).

Appendix A. Supplementary data

Supplementary data to this article can be found online at https://doi.org/10.1016/j.jpowsour.2025.237345.

Data availability

Data will be made available on request.

References

[1] K. Lourenssen, J. Williams, F. Ahmadpour, R. Clemmer, S. Tasnim, Vanadium redox flow batteries: a comprehensive review, J. Energy Storage 25 (2019) 100844, https://doi.org/10.1016/j.est.2019.100844.

[2] K.J. Kim, M.-S. Park, Y.-J. Kim, J.H. Kim, S.X. Dou, M. Skyllas-Kazacos, A technology review of electrodes and reaction mechanisms in vanadium redox flow batteries, J. Mater. Chem. A Mater. 3 (2015) 16913–16933, https://doi.org/10.1039/C5TA02613J.

[3] T.X. Huong Le, M. Bechelany, M. Cretin, Carbon felt based-electrodes for energy and environmental applications: a review, Carbon N Y 122 (2017) 564–591, https://doi.org/10.1016/j.carbon.2017.06.078.

[4] M. Schilling, L. Eifert, K. Köble, M. Jaugstetter, N. Bevilacqua, K.F. Fahy, K. Tschulik, A. Bazylak, R. Zeis, Investigating the influence of treatments on carbon felts for vanadium redox flow batteries, ChemSusChem 17 (2024) e202301063, https://doi.org/10.1002/cssc.202301063.

[5] L. Eifert, Z. Jusys, R.J. Behm, R. Zeis, Side reactions and stability of pre-treated carbon felt electrodes for vanadium redox flow batteries: a DEMS study, Carbon N Y 158 (2020) 580–587, https://doi.org/10.1016/j.carbon.2019.11.029.

[6] B. Sun, M. Skyllas-Kazacos, Modification of graphite electrode materials for vanadium redox flow battery application—I. Thermal treatment, Electrochim. Acta 37 (1992) 1253–1260, https://doi.org/10.1016/0013-4686(92)85064-R.

[7] G.B. Kauffman, Rayon: the first semi-synthetic fiber product, J. Chem. Educ. 70 (1993) 887, https://doi.org/10.1021/ed070p887.

[8] M.P. Vocht, R. Beyer, P. Thomasic, A. Müller, A. Ota, F. Hermanutz, M. R. Buchmeiser, High-performance cellulosic filament fibers prepared via dry-jet wet spinning from ionic liquids, Cellulose 28 (2021) 3055–3067, https://doi.org/10.1007/s10570-021-03697-x.

[9] E. Frank, F. Hermanutz, M.R. Buchmeiser, Carbon fibers: precursors, manufacturing, and properties, Macromol. Mater. Eng. 297 (2012) 493–501, https://doi.org/10.1002/mame.201100406.

[10] S. Zhong, C. Padeste, M. Kazacos, M. Skyllas-Kazacos, Comparison of the physical, chemical and electrochemical properties of rayon- and polyacrylonitrile-based graphite felt electrodes, J. Power Sources 45 (1993) 29–41, https://doi.org/10.1016/0378-7753(93)80006-B.

[11] E. Fitzer, Pan-based carbon fibers—present state and trend of the technology from the viewpoint of possibilities and limits to influence and to control the fiber properties by the process parameters, Carbon N Y 27 (1989) 621–645, https://doi.org/10.1016/0008-6223(89)90197-8.

[12] B.A. Newcomb, Processing, structure, and properties of carbon fibers, Compos Part A Appl Sci Manuf 91 (2016) 262–282, https://doi.org/10.1016/j.compositesa.2016.10.018.

[13] J. Li, Y. Yu, H. Li, Y. Liu, Polyacrylonitrile based carbon fibers: spinning technology dependent precursor fiber structure and its successive transformation, J. Appl. Polym. Sci. 138 (2021), https://doi.org/10.1002/app.50988.

[14] M. Zhang, A.A. Ogale, Carbon fibers from dry-spinning of acetylated softwood kraft lignin, Carbon N Y 69 (2014) 626–629, https://doi.org/10.1016/j.carbon.2013.12.015.

[15] L. Eifert, R. Banerjee, Z. Jusys, R. Zeis, Characterization of carbon felt electrodes for vanadium redox flow batteries: impact of treatment methods, J. Electrochem. Soc. 165 (2018) A2577–A2586, https://doi.org/10.1149/2.0531811jes.

[16] N. Bevilacqua, L. Eifert, R. Banerjee, K. Köble, T. Faragó, M. Zuber, A. Bazylak, R. Zeis, Visualization of electrolyte flow in vanadium redox flow batteries using synchrotron X-ray radiography and tomography – impact of electrolyte species and

electrode compression, J. Power Sources 439 (2019) 227071, https://doi.org/10.1016/j.jpowsour.2019.227071.

[17] K. Köble, M. Jaugstetter, M. Schilling, M. Braig, T. Diemant, K. Tschulik, R. Zeis, Multimodal characterization of carbon electrodes' thermal activation for vanadium redox flow batteries, J. Power Sources 569 (2023) 233010, https://doi.org/10.1016/j.jpowsour.2023.233010.

[18] K. V Greco, A. Forner-Cuenca, A. Mularczyk, J. Eller, F.R. Brushett, Elucidating the nuanced effects of thermal pretreatment on carbon paper electrodes for vanadium redox flow batteries, ACS Appl. Mater. Interfaces 10 (2018) 44430–44442, https://doi.org/10.1021/acsami.8b15793.

[19] A.M. Pezeshki, J.T. Clement, G.M. Veith, T.A. Zawodzinski, M.M. Mench, High performance electrodes in vanadium redox flow batteries through oxygen-enriched thermal activation, J. Power Sources 294 (2015) 333–338, https://doi.org/10.1016/j.jpowsour.2015.05.118.

[20] K.J. Kim, M.-S. Park, J.-H. Kim, U. Hwang, N.J. Lee, G. Jeong, Y.-J. Kim, Novel catalytic effects of Mn3O4 for all vanadium redox flow batteries, Chem. Commun. 48 (2012) 5455–5457, https://doi.org/10.1039/C2CC31433A.

[21] Z. He, Y. Jiang, Y. Wei, C. Zhao, F. Jiang, L. Li, H. Zhou, W. Meng, L. Wang, L. Dai, N,P co-doped carbon microsphere as superior electrocatalyst for VO2+/VO2+ redox reaction, Electrochim. Acta 259 (2018) 122–130, https://doi.org/10.1016/j.electacta.2017.10.169.

[22] D. Dixon, D.J. Babu, J. Langner, M. Bruns, L. Pfaffmann, A. Bhaskar, J.J. Schneider, F. Scheiba, H. Ehrenberg, Effect of oxygen plasma treatment on the electrochemical performance of the rayon and polyacrylonitrile based carbon felt for the vanadium redox flow battery application, J. Power Sources 332 (2016) 240–248, https://doi.org/10.1016/j.jpowsour.2016.09.070.

[23] J. Maruyama, T. Hasegawa, S. Iwasaki, T. Fukuhara, M. Nogami, Mechanism of dioxovanadium ion reduction on oxygen-enriched carbon surface, J. Electrochem. Soc. 160 (2013) A1293–A1298, https://doi.org/10.1149/2.108308jes.

[24] Y. Li, J. Parrondo, S. Sankarasubramanian, V. Ramani, Impact of surface Carbonyl- and hydroxyl-group concentrations on electrode kinetics in an all-vanadium redox flow battery, J. Phys. Chem. C 123 (2019) 6370–6378, https://doi.org/10.1021/acs.jpcc.8b11874.

[25] M. Schilling, R. Zeis, Investigating the V(II)/V(III) electrode reaction in a vanadium redox flow battery – a distribution of relaxation times analysis, Electrochim. Acta 477 (2024) 143771, https://doi.org/10.1016/j.electacta.2024.143771.

[26] M. Schilling, M. Braig, K. Köble, R. Zeis, Investigating the V(IV)/V(V) electrode reaction in a vanadium redox flow battery – a distribution of relaxation times analysis, Electrochim. Acta 430 (2022) 141058, https://doi.org/10.1016/j.electacta.2022.141058.

[27] M. Zago, A. Casalegno, Physically-based impedance modeling of the negative electrode in all-vanadium redox flow batteries: insight into mass transport issues, Electrochim. Acta 248 (2017) 505–517, https://doi.org/10.1016/j.electacta.2017.07.166.

[28] A.M. Pezeshki, Z.J. Tang, C. Fujimoto, C.-N. Sun, M.M. Mench, T.A. Zawodzinski, Full cell study of diels alder poly(phenylene) anion and cation exchange membranes in vanadium redox flow batteries, J. Electrochem. Soc. 163 (2016) A5154–A5162, https://doi.org/10.1149/2.0201601jes.

[29] S. Jeong, L.-H. Kim, Y. Kwon, S. Kim, Effect of nafion membrane thickness on performance of vanadium redox flow battery, Kor. J. Chem. Eng. 31 (2014) 2081–2087, https://doi.org/10.1007/s11814-014-0157-5.

[30] I. Mustafa, I. Lopez, H. Younes, R.A. Susantyoko, R.A. Al-Rub, S. Almheiri, Fabrication of freestanding sheets of multiwalled carbon nanotubes (buckypapers) for vanadium redox flow batteries and effects of fabrication variables on electrochemical performance, Electrochim. Acta 230 (2017) 222–235, https://doi.org/10.1016/j.electacta.2017.01.186.

[31] L. Zhou, W. Zhou, H. Wang, Q. Deng, X. Ai, X.-X. Zeng, X. Wu, C. Zhou, W. Ling, In-situ constructed interface buffer layer enabled highly reversible Zn deposition/stripping for long-lifespan aqueous zinc metal anodes, Chem. Eng. J. 492 (2024) 152324, https://doi.org/10.1016/j.cej.2024.152324.

[32] M. Schilling, A. Ershov, R. Debastiani, K. Duan, K. Köble, S. Scherer, L. Lan, A. Rampf, T. Faragó, M. Zuber, A. Cecilia, S. Liu, C. Liu, T. Baumbach, J. Li, P.-C. Sui, R. Zeis, Bamboo charcoal as electrode material for vanadium redox flow batteries, Energy Adv. 3 (2024) 997–1008, https://doi.org/10.1039/D4YA00166D.

[33] R. Banerjee, N. Bevilacqua, A. Mohseninia, B. Wiedemann, F. Wilhelm, J. Scholta, R. Zeis, Carbon felt electrodes for redox flow battery: impact of compression on transport properties, J. Energy Storage 26 (2019) 100997, https://doi.org/10.1016/j.est.2019.100997.

[34] S. Yadav, M.D.R. Kok, A. Forner-Cuenca, K.M. Tenny, Y.-M. Chiang, F.R. Brushett, R. Jervis, P.R. Shearing, D. Brett, E.P.L. Roberts, J.T. Gostick, Fabrication of high surface area ribbon electrodes for use in redox flow batteries via coaxial electrospinning, J. Energy Storage 33 (2021) 102079, https://doi.org/10.1016/j.est.2020.102079.

[35] M.C. Ribadeneyra, L. Grogan, H. Au, P. Schlee, S. Herou, T. Neville, P.L. Cullen, M. D.R. Kok, O. Hosseinaei, S. Danielsson, P. Tomani, M.M. Titirici, D.J.L. Brett, P. R. Shearing, R. Jervis, A.B. Jorge, Lignin-derived electrospun freestanding carbons as alternative electrodes for redox flow batteries, Carbon N Y 157 (2020) 847–856, https://doi.org/10.1016/j.carbon.2019.11.015.

[36] J. Sun, M.C. Wu, X.Z. Fan, Y.H. Wan, C.Y.H. Chao, T.S. Zhao, Aligned microfibers interweaved with highly porous carbon nanofibers: a novel electrode for high-power vanadium redox flow batteries, Energy Storage Mater. 43 (2021) 30–41, https://doi.org/10.1016/j.ensm.2021.08.034.

[37] Y. Zhao, Y. Li, M. Ihsan-ul-haq, N. Mubarak, M. Xu, X. Qin, T.-S. Zhao, J.-K. Kim, Highly porous carbon nanofiber electrodes for vanadium redox flow batteries, Nanoscale 14 (2022) 5804–5813, https://doi.org/10.1039/D1NR08376G.

[38] X. Li, F. Tian, X. Gao, F. Bian, X. Li, J. Wang, WAXD/SAXS study and 2D fitting (SAXS) of the microstructural evolution of PAN-based carbon fibers during the pre-oxidation and carbonization process, N. Carbon Mater. 32 (2017) 130–136, https://doi.org/10.1016/S1872-5805(17)60110-0.

[39] W. Yang, J. Li, D. Ye, X. Zhu, Q. Liao, Bamboo charcoal as a cost-effective catalyst for an air-cathode of microbial fuel cells, Electrochim. Acta 224 (2017) 585–592, https://doi.org/10.1016/j.electacta.2016.12.046.

[40] S.-J. Park, M.-K. Seo, Y.-S. Lee, Surface characteristics of fluorine-modified PAN-based carbon fibers, Carbon N Y 41 (2003) 723–730, https://doi.org/10.1016/S0008-6223(02)00384-6.

[41] C. Gao, N. Wang, S. Peng, S. Liu, Y. Lei, X. Liang, S. Zeng, H. Zi, Influence of Fenton's reagent treatment on electrochemical properties of graphite felt for all vanadium redox flow battery, Electrochim. Acta 88 (2013) 193–202, https://doi.org/10.1016/j.electacta.2012.10.021.

[42] L. Yue, W. Li, F. Sun, L. Zhao, L. Xing, Highly hydroxylated carbon fibres as electrode materials of all-vanadium redox flow battery, Carbon N Y 48 (2010) 3079–3090, https://doi.org/10.1016/j.carbon.2010.04.044.

[43] I. Derr, D. Przyrembel, J. Schweer, A. Fetyan, J. Langner, J. Melke, M. Weinelt, C. Roth, Electroless chemical aging of carbon felt electrodes for the all-vanadium redox flow battery (VRFB) investigated by electrochemical impedance and X-ray photoelectron spectroscopy, Electrochim. Acta 246 (2017) 783–793, https://doi.org/10.1016/j.electacta.2017.06.050.

[44] L. Eifert, N. Bevilacqua, K. Köble, K. Fahy, L. Xiao, M. Li, K. Duan, A. Bazylak, P.-C. Sui, R. Zeis, Synchrotron X-ray radiography and tomography of vanadium redox flow batteries-cell design, electrolyte flow geometry, and gas bubble formation, ChemSusChem 13 (2020) 3154–3165, https://doi.org/10.1002/cssc.202000541.

[45] O.R.S. (ORS) Inc., Dragonfly: 3D visualization and analysis solutions for scientific and industrial data. http://www.theobjects.com/dragonfly/, 2022.

[46] P. Scherrer, Bestimmung Der Grosse Und Inneren Struktur Von Kolloidteilchen Mittels Rontgenstrahlen, Nach Ges Wiss Gottingen, 1918, pp. 8–100.

[47] T.H. Wan, M. Saccoccio, C. Chen, F. Ciucci, Influence of the discretization methods on the distribution of relaxation times deconvolution: implementing radial basis functions with DRTtools, Electrochim. Acta 184 (2015) 483–499, https://doi.org/10.1016/j.electacta.2015.09.097.

[48] K. Köble, A. Ershov, K. Duan, M. Schilling, A. Rampf, A. Cecilia, T. Faragó, M. Zuber, T. Baumbach, R. Zeis, Insights into the hydrogen evolution reaction in vanadium redox flow batteries: a synchrotron radiation based X-ray imaging study, J. Energy Chem. 91 (2024) 132–144, https://doi.org/10.1016/j.jechem.2023.12.010.

[49] F. Hermanutz, M.P. Vocht, M.R. Buchmeiser, Development of New Cellulosic Fibers and Composites Using Ionic Liquid Technology, 2020, pp. 227–259, https://doi.org/10.1007/978-3-030-35245-5_10.

[50] M.P. Vocht, A. Ota, E. Frank, F. Hermanutz, M.R. Buchmeiser, Preparation of cellulose-derived carbon fibers using a new reduced-pressure stabilization method, Ind. Eng. Chem. Res. 61 (2022) 5191–5201, https://doi.org/10.1021/acs.iecr.2c00265.

[51] A. Ota, R. Beyer, U. Hageroth, A. Müller, P. Tomasic, F. Hermanutz, M. R. Buchmeiser, Chitin/cellulose blend fibers prepared by wet and dry-wet spinning, Polym. Adv. Technol. 32 (2021) 335–342, https://doi.org/10.1002/pat.5089.

[52] T. Tagawa, T. Miyata, Size effect on tensile strength of carbon fibers, Mater. Sci. Eng. 238 (1997) 336–342, https://doi.org/10.1016/S0921-5093(97)00454-1.

[53] F.W. Zok, On weakest link theory and weibull statistics, J. Am. Ceram. Soc. 100 (2017) 1265–1268, https://doi.org/10.1111/jace.14665.

[54] P.L. de Andres, R. Ramírez, J.A. Vergés, Strong covalent bonding between two graphene layers, Phys. Rev. B 77 (2008) 045403, https://doi.org/10.1103/PhysRevB.77.045403.

[55] X. Zhang, S. Fujiwara, M. Fujii, Measurements of thermal conductivity and electrical conductivity of a single carbon fiber, Int. J. Thermophys. 21 (2000) 965–980, https://doi.org/10.1023/A:1006674510648.

[56] E.A. Belenkov, Formation of graphite structure in carbon crystallites, Inorg. Mater. 37 (2001) 928–934, https://doi.org/10.1023/A:1011601915600.

[57] K. Köble, L. Eifert, N. Bevilacqua, K.F. Fahy, A. Bazylak, R. Zeis, Synchrotron X-Ray radiography of vanadium redox flow batteries – Time and spatial resolved electrolyte flow in porous carbon electrodes, J. Power Sources 492 (2021) 229660, https://doi.org/10.1016/j.jpowsour.2021.229660.

[58] K. Köble, M. Schilling, L. Eifert, N. Bevilacqua, K.F. Fahy, P. Atanassov, A. Bazylak, R. Zeis, Revealing the Multifaceted Impacts of Electrode Modifications for Vanadium Redox Flow Battery Electrodes, ACS Appl. Mater. Interfaces 15 (2023) 46775–46789. https://doi.org/10.1021/acsami.3c07940.

[59] P.C. Ghimire, R. Schweiss, G.G. Scherer, T.M. Lim, N. Wai, A. Bhattarai, Q. Yan, Optimization of thermal oxidation of electrodes for the performance enhancement in all-vanadium redox flow betteries, Carbon N Y 155 (2019) 176–185, https://doi.org/10.1016/j.carbon.2019.08.068.

[60] K.V. Greco, J.K. Bonesteel, N. Chanut, C. Tai-Chieh Wan, Y.-M. Chiang, F. R. Brushett, Limited accessibility to surface area generated by thermal pretreatment of electrodes reduces its impact on redox flow battery performance, ACS Appl. Energy Mater. 4 (2021) 13516–13527, https://doi.org/10.1021/acsaem.1c01980.

[61] K. Köble, M. Schilling, L. Eifert, N. Bevilacqua, K.F. Fahy, P. Atanassov, A. Bazylak, R. Zeis, Revealing the multifaceted impacts of electrode modifications for vanadium redox flow battery electrodes, ACS Appl. Mater. Interfaces 15 (2023) 46775–46789, https://doi.org/10.1021/acsami.3c07940.